J. Fluid Mech. (1971), *vol.* 47, *part* 3, *pp.* 481–502
Printed in Great Britain

Turbulent flow in wavy pipes

By SHENG-TIEN HSU† AND JOHN F. KENNEDY
Institute of Hydraulic Research, The University of Iowa, Iowa City, Iowa

(Received 3 July 1969 and in revised form 1 July 1970)

A primarily experimental investigation was undertaken to determine the internal structure of steady, quasi-uniform, non-separated, axisymmetric flows in circular pipes with sinusoidal wall profiles. The quantities measured include radial and longitudinal distributions of mean velocity, pressure, and total head; the Reynolds shear stress and all three components of turbulence velocity; and boundary shear stress and pressure. Two different wall-wave steepnesses were investigated, and a constant Reynolds number of $1{\cdot}13 \times 10^5$ (based on the average pipe diameter) was maintained in most experiments. The boundary shear stress was found to be shifted upstream relative to the boundary wave, whereas the wall pressure is shifted slightly downstream. The turbulence measurements revealed that there is a central core extending over some 60 % of the pipe radius in which the turbulence quantities are constant along the pipe. Near the boundary, however, the turbulence velocities and stress vary periodically along the boundary waves. The longitudinal component of mean velocity was found to be distributed radially according to the power law, but with an exponent that varies along each wave; a simple analytical model is constructed to predict the variation of the exponent. It was not found possible to relate the local boundary shear stress to just the local flow characteristics, since the convective or 'history' effects play a significant role in its determination. An empirical formula is derived relating the local boundary shear stress to the local velocity distribution and the first two derivatives of the boundary profile.

1. Introductory remarks

Shear flows past wavy boundaries have attracted considerable research attention in recent years because of the central role they play in several intriguing phenomena: the generation of wind waves on water; the formation of sedimentary ripples and dunes in deserts and river channels; the stability of a liquid film in contact with a gas stream; and the rippling of melting surfaces. Wavy-boundary flows of gases in chemical or vibrational non-equilibrium have also been treated at some length (Vincenti 1959; Rhyming 1963). A concise review of this general class of problems has been given by Benjamin (1959). Experimental determination of the internal structure of wavy-boundary flows is generally complicated by secondary effects. For example, free-surface flows over wavy beds are accompanied by relatively strong secondary currents generated by the interaction

† Present address: Tennessee Valley Authority Hydraulic Laboratory, Norris, Tennessee

between streamline curvature in vertical planes and the velocity gradient outward from the plane side-walls of the flume, and at higher Froude numbers by diagonal standing waves (Robillard & Kennedy 1967). Wavy-bed flows in rectangular cross-section ducts, as investigated by Motzfeld (1937), must also give rise to centrifugally induced secondary currents. Air flows over progressive water-waves are experimentally troublesome because of their unsteadiness.

The purpose of the primarily experimental investigation reported herein was to obtain detailed data on both mean-flow properties and turbulence characteristics for the simplest realizable wavy-boundary shear flow: steady, quasi-uniform, non-separated, axisymmetric flow in a circular pipe, the diameter of which varies sinusoidally along its length. This flow is ideally two-dimensional, generates no secondary currents (except perhaps for Goertler vortices), and offers the additional advantage that there are already available for reference adequate data on the limiting case in which the wave steepness tends to zero. Measurements were obtained for two different test sections with the same wave amplitude and average† diameter, but with wavelengths differing by a factor of two. The same Reynolds number, $1{\cdot}13 \times 10^5$ based on the average pipe diameter, was maintained throughout the investigation, except for some auxiliary experiments performed to ascertain the effect of Reynolds number on the boundary shear stress. The quantities measured and reported in the following sections include radial and longitudinal distributions of mean velocity, pressure, and total head; the Reynolds shear stress and all three components of turbulence velocities; and boundary shear stress and pressure. A simple analytical model is developed for predicting the variation along the pipe of the form of the mean-velocity profile, and an empirical relation is derived relating the local boundary shear velocity to the local flow characteristics and conduit geometry.

2. Experimental apparatus

The experimental set-up is depicted schematically in figure 1 (*a*). The air flow supplied by the centrifugal blower was discharged into a 4 ft diameter chamber which contained four layers of $\frac{1}{2}$-inch mesh screen. The necessary steps were taken to isolate the blower and stilling chamber to prevent objectionable vibration of the approach pipe and test section. A Prandtl tube located at the pipe centreline near the downstream end of the contraction section was used to ensure that the desired discharge was maintained in all tests. The 20 ft long approach pipe provided fully developed flow at the inlet to the test section. The honeycomb and screens at the upstream end of the approach pipe were required to obtain an axisymmetric velocity distribution at the instrument-port section near the downstream end of the approach pipe. The mean-velocity distributions measured in two perpendicular planes at this section were found to be congruent and symmetric about the pipe axis, and to have the power-law form with an inverse exponent, $n = 6{\cdot}7$, in the range one would expect for the Reynolds number of the flow.

† Herein, the term 'average' refers to values taken along the pipe, while 'mean' designates values measured over a cross-section or at a point over a period of time.

Table 1 summarizes the geometrical characteristics of the two wavy test sections used. The section numbers referred to in subsequent discussion are identified in figure 1 (*b*).

To obtain an indication of the maximum value of a/L which could be expected to be free from local separation, some ancillary experiments were made in an open-throat wind tunnel using a series of 4 in. average diameter axisymmetric

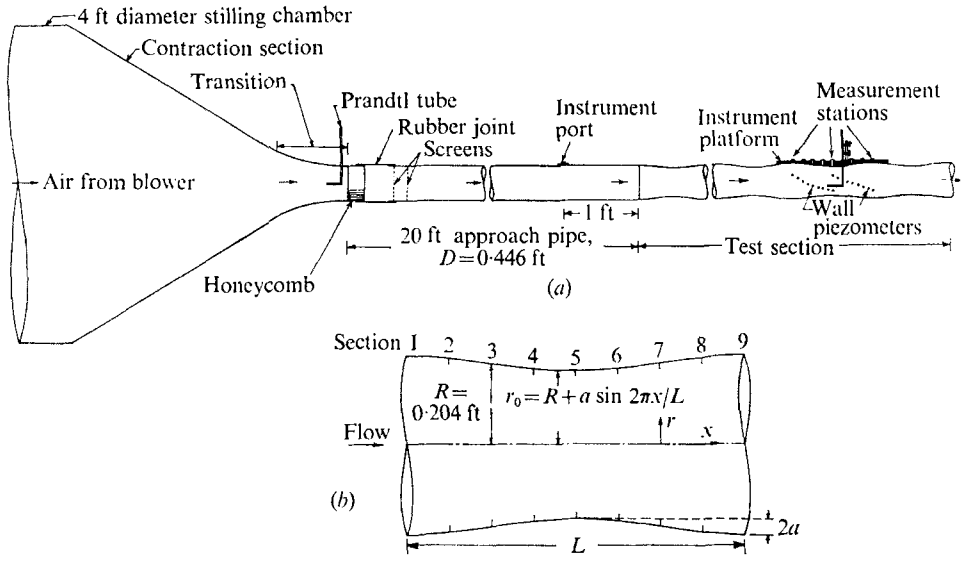

FIGURE 1. (*a*) Schematic diagram of experimental set up, and (*b*) definition sketch of instrumented wave.

Model	D Average diameter (ft)	a Wave amplitude (ft)	L Wave-length (ft)	a/L	No. of waves	Total length (ft)	Measure-ments made on section at wave no.†
I	0·408	0·0184	0·833	1/45	10	8·33	8
II	0·408	0·0184	1·667	1/90	6	10·00	5

† Waves numbered from upstream end.

TABLE 1. Geometry of wavy test sections

elongated bodies with rounded upstream ends and sinusoidal longitudinal wall profiles. Separation was detected by painting the bodies with a mixture of lamp-black and kerosene. Four wave steepnesses were tested: $a/L = 1/20$, $1/25$, $1/35$ and $1/45$. Separation appeared to be just incipient on the body with $a/L = 1/35$, while the one with $a/L = 1/45$ gave no indication of separation; hence the latter value was selected for the first wavy pipe fabricated. The wavy pipes were constructed by forming fibreglass on to machined wooden mandrels. Each wavy pipe was fitted with two longitudinal flanges, so the half-sections could be separated

along a diametrical plane. A transparent window was provided along the wave in which the measurements were made, to permit observation of the measuring probes. Measurement ports were machined at intervals of $\frac{1}{4}\pi$ along one wavelength into a resin instrument platform cast on to the wavy pipe. Probes were supported by a rack and pinion which was equipped with a vernier and which could be moved along the metal track attached to the instrument platform. It was verified that the probes did in fact traverse a diameter. Some additional measurement ports were installed later for detailed measurements of boundary shear-stress distribution, which were made to determine more precisely the phase shift between the shear stress and the wall profile. When a port was not being used it was closed with a plug, the face of which was hand finished to give a smooth surface to the inner pipe wall. Small diameter piezometer openings for measurement of wall pressure were provided at intervals of $\frac{1}{8}\pi$ along two waves; to minimize interference, each hole was offset tangentially from the adjacent upstream one. The joints at flanges, around windows, etc., were all carefully hand finished to produce a smooth, continuous surface.

Turbulence velocities and stresses were measured using a linearized-output, two-channel Old Gold Hot-Wire Anemometer and Mean-Product Computer, developed and constructed at the Iowa Institute of Hydraulic Research and described by Glover (1967). A single-wire probe with the wire mounted horizontally and oriented perpendicularly to the pipe axis was used to measure the longitudinal components of both the mean and turbulence velocities. The two specially designed cross-wire probes used to measure the tangential and radial components of velocity had the wires mounted in horizontal and vertical planes, respectively, and oriented at $\pm 45°$ to the pipe axis. Total-head and pressure-head distributions were measured separately with total- and pressure-head tubes so designed that the sensing ports were in the planes of the sections identified in figure 1 (*b*). The mean velocities measured with the total- and static-head tubes, the single-wire probe, and the two cross-wire probes were compared and found to be in excellent conformity, as were the longitudinal components of the turbulence velocities measured with the three different hot-wire probes. The radial distributions of total-head and pressure-head were found to be symmetric at all test stations, and hence measurements with the hot-wire probes were made only over the radius away from the wall in which the probes were mounted; the hot-wire probe supports were designed accordingly to permit measurements very close to the wall.

The mean-velocity profile obtained with the hot wire at each measurement station was integrated (after weighting the measured velocities with the local radii) and the discharges so obtained (which were found to be in excellent agreement) were averaged and used in calculation of the average velocity, Reynolds number, etc. Wall shear stress was measured with a modified Preston tube (*Zweilochsonde*) of the type described by Rechenberg, Schwefel & Bienert (1967); the probe employed is sketched in figure 2. The hypodermic tubing from which the probe tubes were fabricated was sufficiently elastic that the end of the probe could easily be deflected to be tangent to the wall at any station by merely depressing the probe stem with the rack-and-pinion mount. The probe was cali-

brated in the instrument port located at the downstream end of the approach pipe, using measured pressure gradients along the pipe. All pressures and heads were measured with a null-displacement micro-manometer with a discrimination of 0·001 in. of alcohol. The outside diameter of the tubes was sufficiently small (1·0 mm) that errors of not more than a few per cent are suggested by Brown & Joubert's (1969) error-criteria graph for Preston tubes (their figure 9), based on measured values of shear velocity, maximum wall-pressure gradient, etc., in the

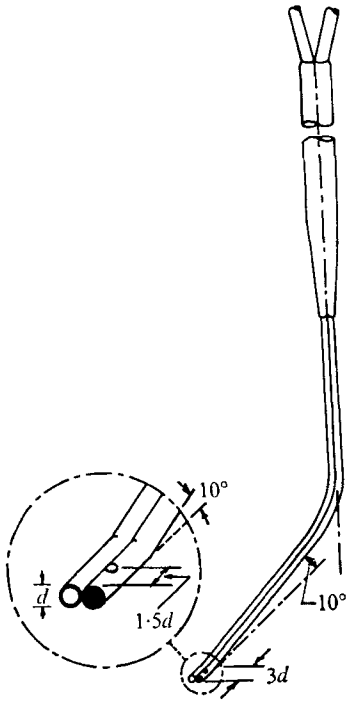

FIGURE 2. Detail of shear-stress probe. d = 1·0 mm.

wavy pipes. The shear velocity-tube diameter Reynolds number varied along the pipe from about 30 to 60, which would indicate that the tubes were contained well within the law-of-the-wall region. Uncertainties about the extent of the law of the wall in strong pressure gradients preclude a more precise evaluation of the accuracy of the boundary shear-stress measurements.

3. Presentation of results

The same mean velocity, U = 46·7 ft/sec (based on the average wavy-pipe diameter, 0·408 ft) was used in most of the experiments. Some auxiliary experiments were made with U = 39·5 ft/sec to obtain additional data on the boundary shear-stress distribution. In other supplementary tests, not reported herein, it was found that the normalized mean-velocity profiles were unaltered when the average velocity was increased by some 40 %. Comparisons of the various flow

properties at sections 1 and 9 (see figure 1 (*b*)) will frequently be made in conjunction with discussion of the quasi-uniformity of the flow.

Distributions of total head and pressure

Figure 3 portrays the distributions of total head, referenced to the wall at section 1 and normalized by $U^2/2g$, for models I and II. As would be expected, the boundary convergence from section 1 to section 5 causes the total-head profiles to become flatter, while the divergence from section 5 to section 9 produces progressively sharper profiles. Two noteworthy points should be mentioned here. First, in both models the centreline total head is hardly affected by the convergence and divergence; moreover, at the centreline, the head loss due to

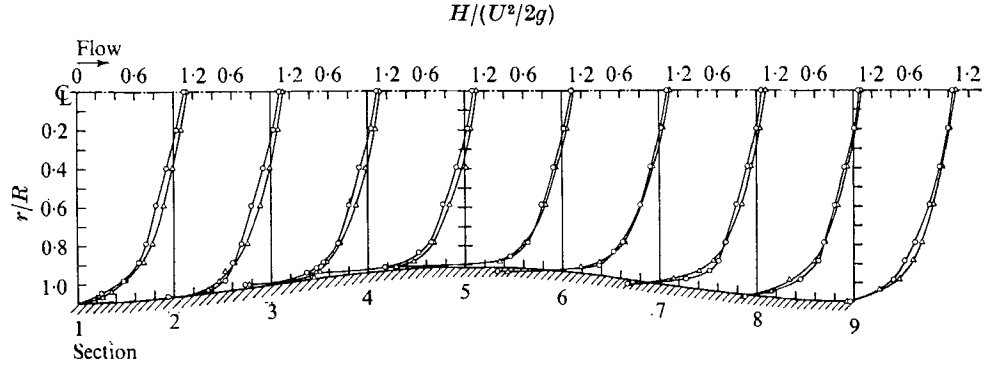

FIGURE 3. Total head profiles. ○, model I; △, model II.

energy dissipation is more or less uniformly distributed. Secondly, the total head profiles at sections 1 and 9 are virtually identical, allowing for a small decrease due to dissipation, suggesting that quasi-uniform flow had been attained at the wave where measurements were made.

Figure 4 presents for both pipes the distributions of pressure normalized by $\frac{1}{2}\rho U^2$. The boundary pressures shown were measured through the wall piezometers. As in figure 3, the reference pressure has been taken to be $p = 0$ at the wall at section 1. The effects of boundary curvature are clearly evident. At sections where the wall is concave (sections 1, 2, 8, 9) the pressure decreases toward the pipe centreline, whereas at sections of convex boundary (sections 4, 5, 6) the converse holds. At the inflexion points (sections 3, 7) the pressure is nearly constant across the pipe. The effects are, of course, more pronounced in model I, which had shorter, steeper waves. Figure 5 shows the distributions of wall pressure, measured through the piezometer taps; the reference pressure has once again been taken to be $p = 0$ at section 1. The pressure wave is seen to be shifted a small distance downstream relative to the boundary undulations. The data presented include no correction for the small pressure drop resulting from dissipation (compare pressures at sections 1 and 9). Even if some estimate of this correction is applied, say by distributing the total pressure drop along the wavelength on the basis of uniform-flow friction factors for the local diameters and velocities, the pressure distributions are still found to be shifted slightly down-

stream. Such a phase shift has been observed experimentally by Motzfeld (1937) in wind-tunnel studies with a two-dimensional wavy bed, and predicted analytically by Benjamin (1959) for the case of shear flow of semi-infinite extent past a wavy boundary. Larras & Claria (1960), on the other hand, observed that the wall pressure is symmetrically disposed with respect to a two-dimensional sinusoidal bed. Benjamin predicted for the simplified (sinusoidal) velocity distri-

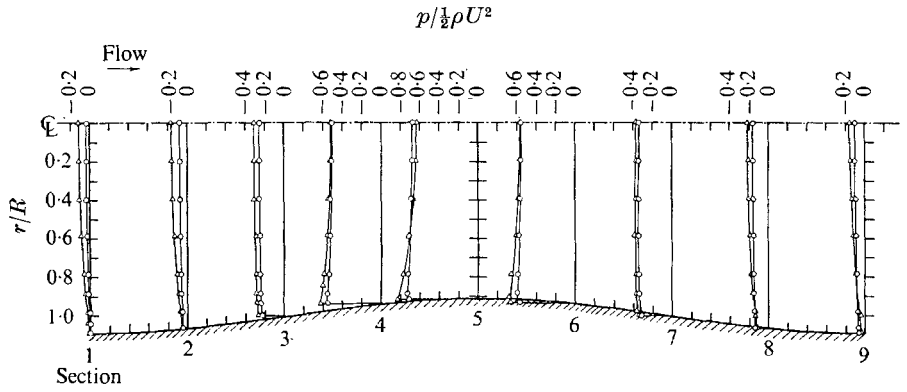

FIGURE 4. Pressure distributions. ○, model I; △, model II.

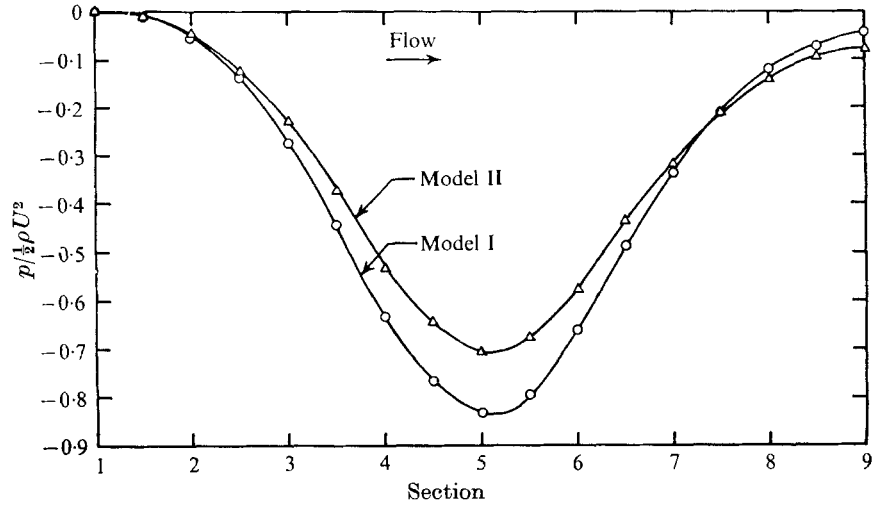

FIGURE 5. Boundary pressure measured through wall piezometers.

bution he considered a boundary pressure phase shift of $\frac{1}{6}\pi$; the phase shifts in the present case are seen to be somewhat less.

Mean-velocity profiles

The mean-velocity profiles for both models are shown in figure 6, and those for model I are presented in a logarithmic plot in figure 7. The convergence and divergence of the section have the anticipated effect on the general shape of the velocity profiles. Figure 7 demonstrates that the mean-velocity profiles at loca-

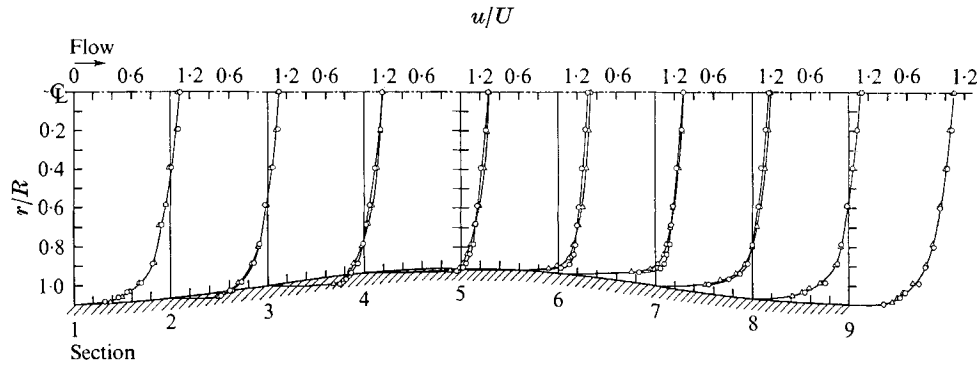

FIGURE 6. Mean velocity profiles. ○, model I; △, model II.

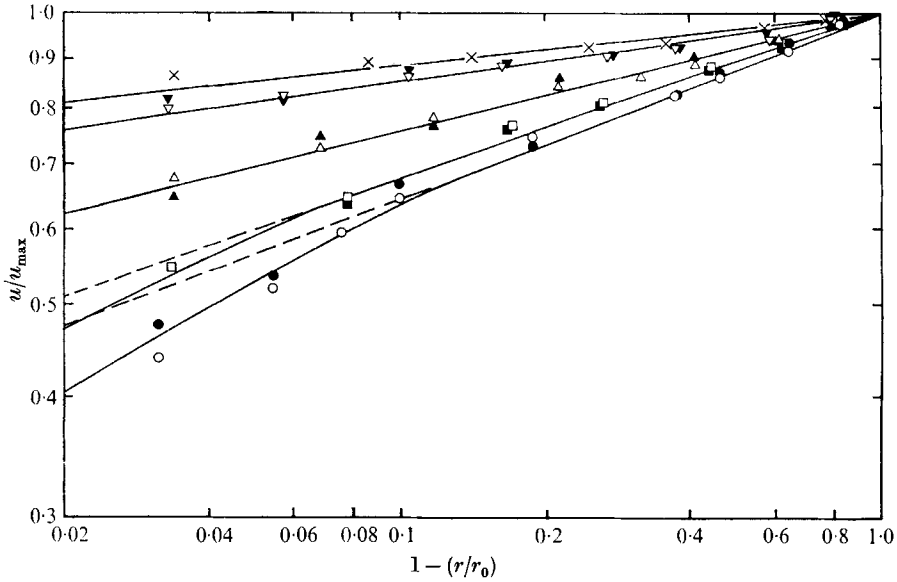

FIGURE 7. Power-law form of velocity distributions, model I. Section: ○, 1; □, 2; △, 3; ▽, 4; ×, 5; ▼, 6; ▲, 7; ■, 8; ●, 9.

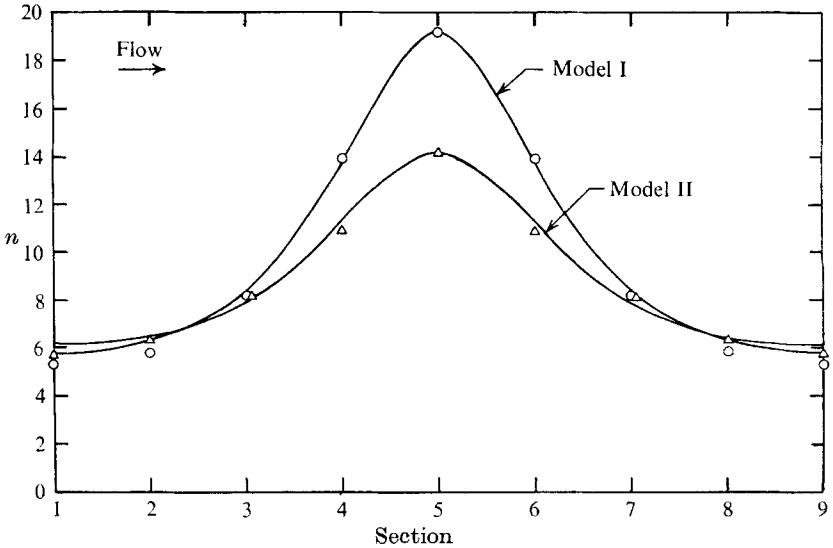

FIGURE 8. Comparison of measured and predicted values of n. Experimental: ○, model I; △, model II. ——, analytical.

tions symmetrical about the section of minimum (or maximum) diameter are nearly identical, the point velocities displaying significant differences only in the immediate vicinity of the wall. Moreover, it is seen that over 90 % or more of the radius at each section the mean velocity is distributed in accordance with the power-law,

$$u/u_{\max} = (1 - r/r_0)^{1/n}, \tag{1}$$

where $u_{\max}$ is the maximum (centreline) velocity at the section and r_0 is the local radius. The mean-velocity data demonstrated a similar degree of conformity to the logarithmic law. Because of the strong non-uniformity of the flow, both n in the power law and Kármán's κ in the logarithmic distribution vary from section to section. Figure 8 shows the values of n determined from figure 7 and a similar plot for model II. The analysis producing the predictions for n is presented in section 5.

Boundary shear stress

The boundary shear stresses measured with the modified Preston tube are presented in figure 9, wherein the shear-stress distributions are seen to be shifted upstream relative to the boundary wave. The phase shifts are approximately

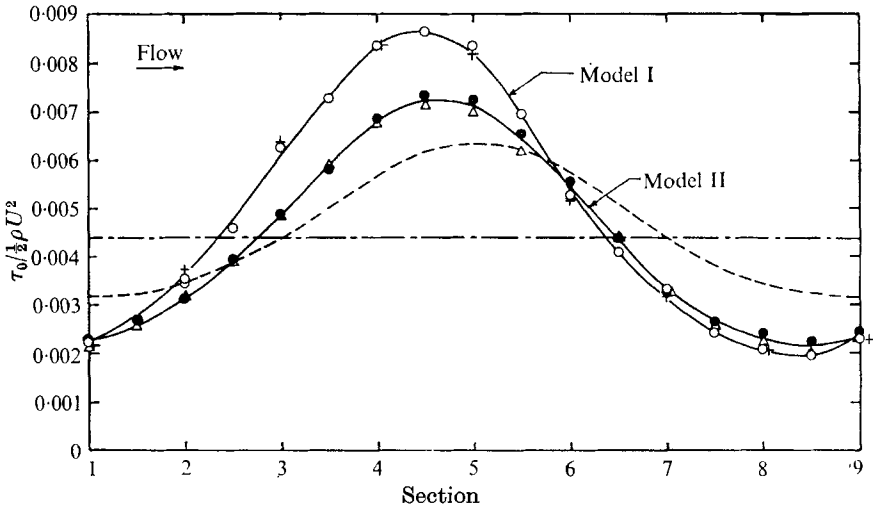

FIGURE 9. Boundary shear-stress distributions. ---, calculated for uniform flow using local diameter; ——, calculated for uniform flow using average diameter. Model I: ○, $Re = 1{\cdot}13 \times 10^5$; +, $Re = 0{\cdot}90 \times 10^5$. Model II: ●, $Re = 1{\cdot}13 \times 10^5$; △, $Re = 0{\cdot}90 \times 10^5$.

$0{\cdot}072L$ (26°) and $0.050L$ (18°) for models I and II, respectively. Benjamin (1959) predicted an upstream phase shift of $\frac{1}{6}\pi$ for the simplified velocity profiles used in his analysis of a semi-infinite stream moving past a wavy bed. The normalized shear stresses calculated using uniform-flow friction factors obtained from the Moody pipe-friction diagram for the average and local velocities and diameters are also shown in figure 9. It is seen that the alternate convergence and divergence produce significant increases in the magnitude of the shear-stress variations. It is also noteworthy that although the radial distributions of mean velocity are

virtually identical at corresponding converging and diverging sections, the shear stress is not symmetrically disposed about the boundary waves; this points up the role of convective effects in determining the local boundary shear stress.

Note that the shear stresses at sections 1 and 9 are equal for each model, giving further testimony to the quasi-uniformity of the flow.

Turbulence intensities

Figures 10 and 11 show the distributions of the r.m.s. of each of the three components of the turbulence velocities for both models, normalized by the calculated shear velocity for a straight pipe with the average diameter of the wavy

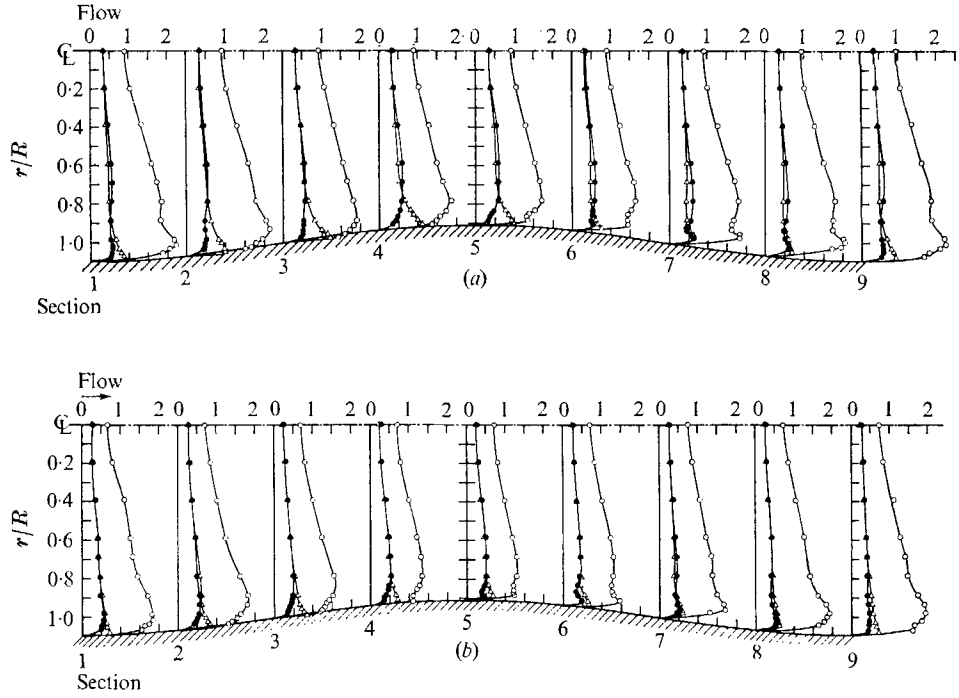

FIGURE 10. Root-mean-square values of components of turbulence velocities. (*a*) Model I. (*b*) Model II. ○, $(\overline{u'^2})^{\frac{1}{2}}/u_{\tau m}$; ●, $(\overline{v'^2})^{\frac{1}{2}}/u_{\tau m}$; △, $(\overline{w'^2})^{\frac{1}{2}}/u_{\tau m}$.

pipes: $u_{\tau m} = 2{\cdot}2$ ft/sec. In figure 11 (*a*)–(*c*) no attempt has been made to delineate the profiles for each section; instead, only some representative and limiting profiles are shown. Also included for reference in figure 11 (*a*)–(*c*) are the turbulence profiles measured by Laufer (1954) at a Reynolds number of 5×10^5 in a smooth uniform pipe. In a straight pipe all three components of the turbulence velocity are equal at the centreline, while in the present case the longitudinal component is larger by a factor of two to three than the other two components. The turbulence intensities in model I are greater by some 20–30 % than those in model II; the increase would be expected from the generally larger shear stress and stronger non-uniformity in model I (see figure 9). The comparison in figure 11 (*a*)–(*c*) of the non-dimensionalized turbulence intensities with those obtained by Laufer (1954)

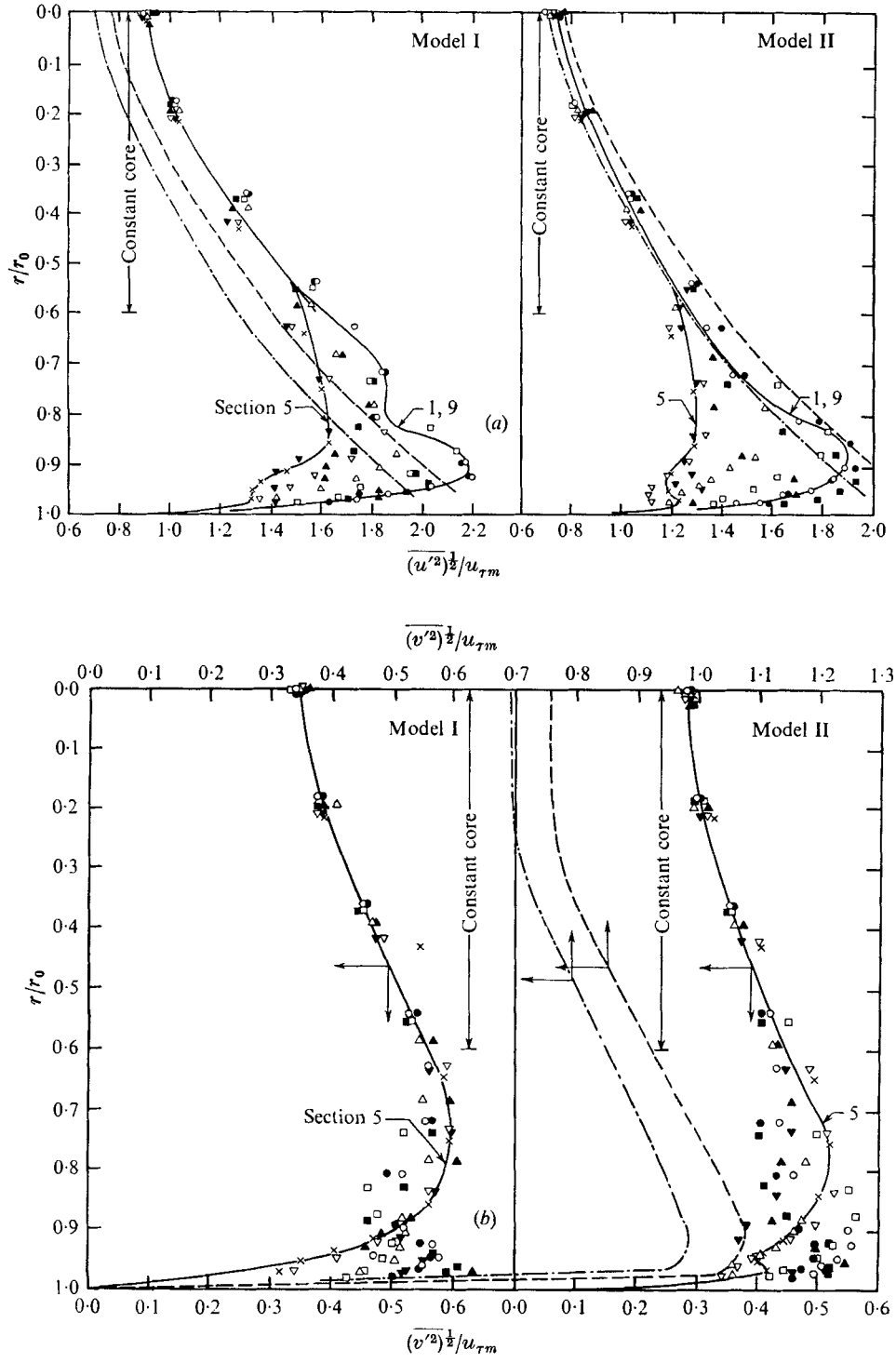

FIGURE 11. For legend see next page.

at corresponding values of the normalized radial co-ordinate reveals that the radial and tangential components are generally less than half as great as those of uniform flow in a pipe with the average wavy-pipe diameter, while the longitudinal component in model I is some 25 % greater than in a straight pipe, and in model II is nearly the same as in a straight pipe. Hence the alternate con-

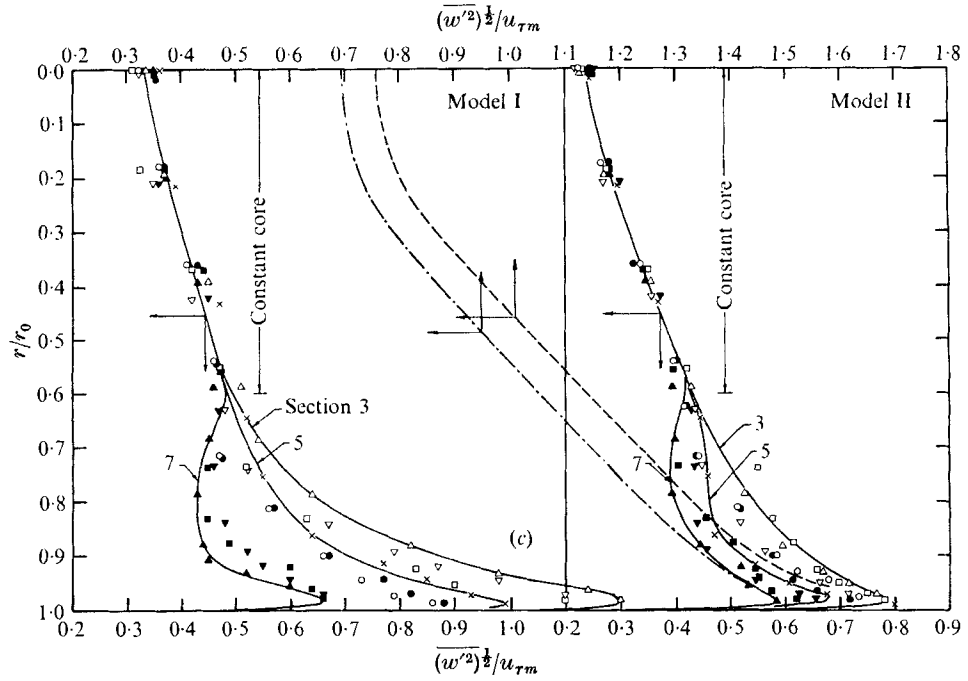

FIGURE 11. Comparative plots of root-mean-square of components of turbulence velocities. (*a*) Longitudinal, (*b*) radial, (*c*) tangential. ——, wavy pipe; — —, uniform pipe with average wavy-pipe diameter (Laufer 1954); —·—, uniform pipe with maximum wavy-pipe diameter (Laufer 1954). Section: ○, 1; □, 2; △, 3; ▽, 4; ×, 5; ▼, 6; ▲, 7; ■, 8; ●, 9.

vergence and divergence of the flow has the net effect of diminishing the radial and tangential components of the turbulence velocity, while the streamwise component may be slightly increased. Perhaps the most interesting aspect of the turbulence structure is portrayed in figure 11 (*a*)–(*c*), wherein it is seen that over a central core covering some 60 % of the radius the turbulence intensities remain virtually constant along the pipe. Outside of the core, in the annular region adjacent to the boundary, the turbulence intensities are strongly influenced by the local boundary shear stress and boundary configuration. The curious irregularities in the turbulence distributions near the wall, as well as other features of the turbulence structure, will be discussed in § 4.

Reynolds stress

In axially symmetric flows, such as those under consideration, it seems reasonable to expect that the only Reynolds shear stress greatly different from zero is that acting on circumferential surfaces, $-\rho\overline{u'v'}$. A few measurements of

$\overline{u'w'}$ confirmed that this quantity is in fact zero in the present flow configuration. Figure 12 shows the radial and longitudinal distributions of $-\rho\overline{u'v'}$, normalized by the average boundary shear stress, and figure 13 presents a comparison of the Reynolds stress profiles for all sections in each model. Also shown in figure 13 are

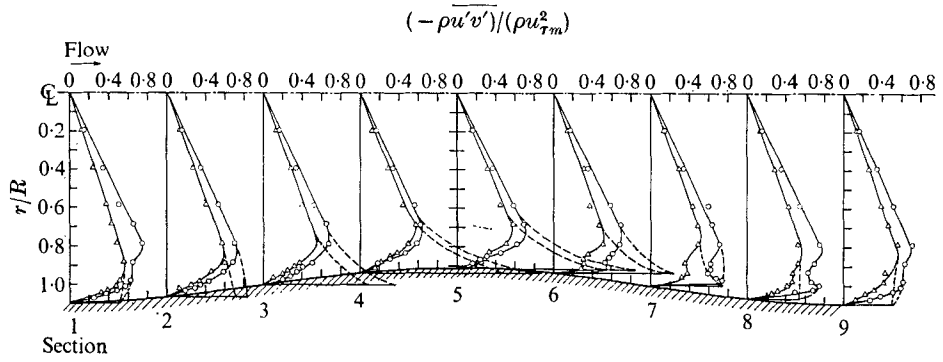

FIGURE 12. Reynolds shear stress distributions. ○, model I; △, model II.

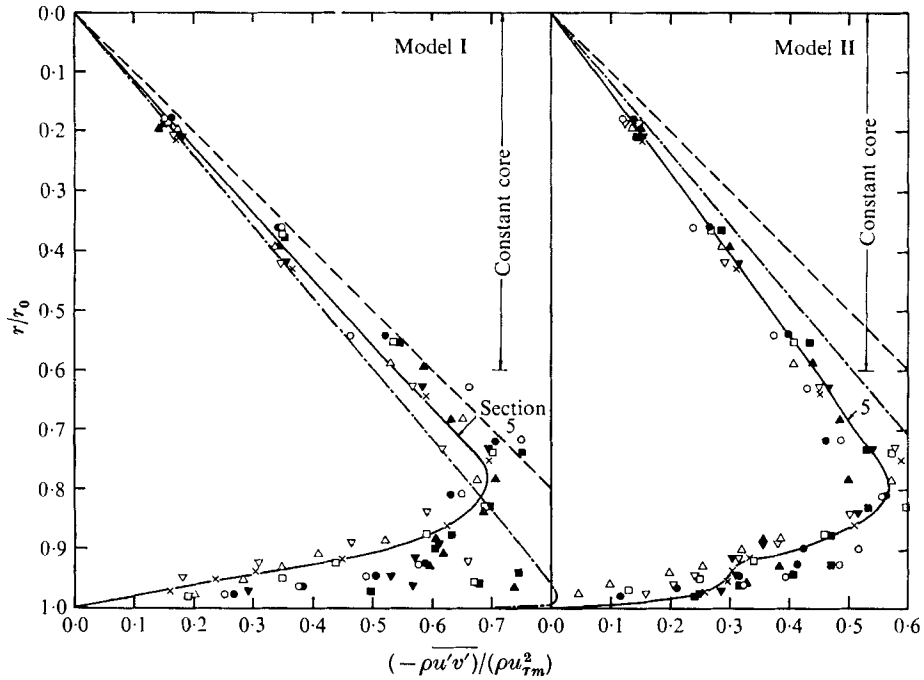

FIGURE 13. Comparative plots of Reynolds shear stress. ——, wavy pipe; – – –, uniform pipe with average wavy-pipe diameter (Laufer 1954); —·—, uniform pipe of maximum wavy-pipe diameter (Laufer 1954). Section: ○, 1; □, 2; △, 3; ▽, 4; ×, 5; ▼, 6; ▲, 7; ■, 8; ●, 9.

the computed shear stresses for uniform pipes with the average and the maximum wavy-pipe diameters. In figure 12 it is seen that the Reynolds stress is generally greater in model I than in model II, in correspondence with the larger boundary shear stress in model I. The core region, in which the turbulence intensities are

nearly constant, that was revealed in figure 11 (*a*)–(*c*) is also characterized by constant shear stress. In model I the constant-core shear stress is intermediate to the values in uniform pipes with the maximum and average wavy-pipe diameters, while in model II it is somewhat less in keeping with the generally lower turbulence levels in this pipe. The irregularities noted in the distributions of turbulence velocities are also present in the Reynolds stress profiles.

4. Discussion of results

Momentum balance

Further consideration of the data presented in figures 3–13 yields some insights that are helpful in gaining a better understanding of wavy boundary flow. First,

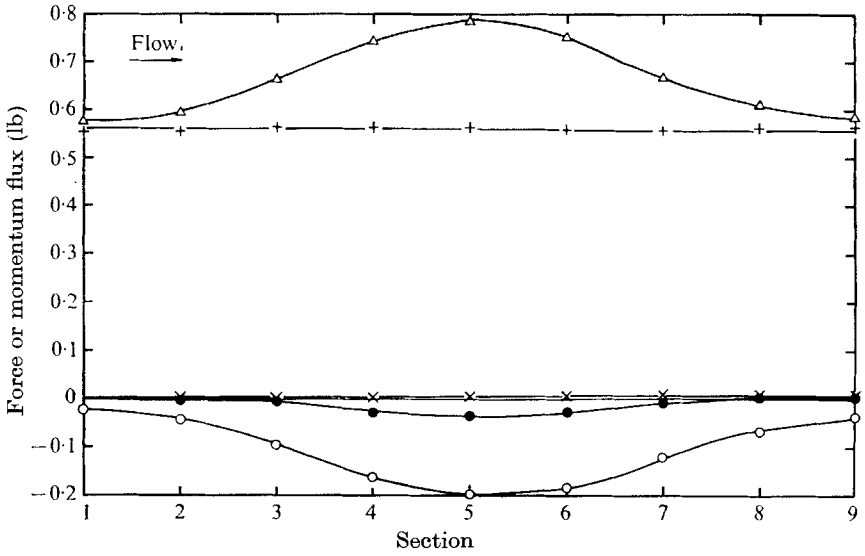

FIGURE 14. Distributions of components of longitudinal momentum balance. △, momentum flux; ×, shear force (integrated from section 1); ●, longitudinal pressure force on boundary (integrated from section 1); ○, pressure force on flow section; +, sum of forces and momentum flux.

it is revealing to examine the magnitudes of the principal contributions to the streamwise momentum balance; these are presented for model I in figure 14, which shows the longitudinal momentum flux and pressure force at each section, the longitudinal components of shear force exerted on the fluid by the wall between section 1 and the downstream sections; and the sum of these four quantities. The measured values of mean velocity, pressure and shear stress were used in calculating the various quantities appearing in this figure. The variation along the pipe in the momentum contribution of the longitudinal component of turbulence was found to be negligible. The sum of the streamwise momentum flux and forces is seen to be very nearly constant at every section; this tends to corroborate the accuracy of the measured data. Next, note that the contributions of the wall-pressure force and especially of the wall-shear force are very small

compared to the variation in the momentum flux and the pressure force exerted across the flow section on the fluid. This implies that variations in the momentum flux are balanced primarily by the pressure force exerted over the cross-section. This consideration also points out the practically insurmountable difficulty encountered in attempting to calculate the local boundary shear stress from a momentum analysis. To do so would require great precision in the estimates of the momentum flux and pressure profiles, and hence accurate estimates also for the velocity profiles—accuracy which cannot presently be attained without very extensive computational effort.

As the flow section converges and diverges along the wavy pipe, the Bernoulli or Venturi effect gives rise to an alternately negative and positive streamwise pressure gradient. The centrifugally induced radial pressure gradients cause this longitudinal pressure gradient to vary radially, increasing in magnitude outward from the centreline. This is apparent in figure 4, wherein it is seen that the radial pressure gradients are such that with increasing r they increase the magnitude of the negative streamwise pressure gradient between sections 1 and 5 and strengthen the adverse pressure gradient between sections 5 and 9. This radial variation of the longitudinal pressure gradient has a marked effect on the mean-velocity profiles, enhancing as it does, with increasing r, the longitudinal acceleration (between sections 1 and 5) and deceleration (between sections 5 and 9). Thus the boundary curvature reinforces the ordinary effects of boundary convergence and divergence on the radial distribution of velocity with the result, demonstrated in figure 6, that the velocity profiles become progressively blunter as the local diameter decreases in the flow direction and sharper in the reaches where the flow section is enlarging. Since the streamwise pressure gradient varies radially, as well as along the pipe, the radial distribution of longitudinal velocity must also change in the flow direction, and it is no longer possible to represent the velocity profiles with a one-parameter family of curves in which the parameter is related only to the boundary convergence or divergence (or the pressure gradient) as is the case for straight-walled non-uniform sections. The variations in the radial distribution of mean velocity affect in turn both the momentum flux and the total pressure force. The first of these effects is relatively small, as can be inferred from the calculations presented by Iwasa & Kennedy (1968), while the second is much more significant since the details of the velocity distribution near the boundary, where the streamline curvature is greatest, have a pronounced effect on the total pressure force. This latter effect is magnified in the case of a circular pipe by both the incremental area corresponding to each element of radius and the longitudinal pressure gradient increasing with r.

Turbulence velocities

The distributions of turbulence velocities and turbulence shear stress shown in figures 10 to 13 raise several questions. First, it is difficult to reconcile the existence of the constant core, throughout which the turbulence does not vary in the streamwise direction, with the results of rapid distortion theory (Taylor 1935; Batchelor & Proudman 1954). For example, Batchelor & Proudman's calculation of the effect of a symmetrical contraction on turbulence intensities predicts

that in the present flows, $(\overline{u'^2})^{\frac{1}{2}}$ is diminished between sections 1 and 5 by approximately 25 %, while the other two turbulence velocity components are increased by a comparable factor. To be sure, the restrictions imposed in Batchelor & Proudman's analysis (rapid distortion, homogeneous turbulence, viscous effects neglected) were not met in the present experiments, but one might have expected the experimental and theoretical results to be at least qualitatively similar. In the vicinity of the wall, u' does attain its minimum values at the ends of the contracting reaches (section 5), and its maxima near the end of the expansions (sections 1 and 9), as is shown in figure 11 (*a*). Close examination of figure 11 (*c*) reveals that near the boundary the maxima and minima of w' occur near stations 3 and 7, respectively, while for v' (figure 11 (*b*)) there is no discernible consistent pattern outside the constant core. One might conjecture that the seemingly erratic behaviour of v' near the wall is the result of Goertler vortices, but if this were the case the distribution of w' should be equally irregular.

The turbulence configuration of this flow is affected not only by distortion, but also by the production, transport and dissipation of turbulence energy. The streamwise variation in the boundary shear stress with its attendant effect on the turbulence production must be responsible in large part for the seemingly erratic radial distributions of turbulence intensity near the boundaries. Turbulence produced near the wall is generally transported radially inward, dissipating as it diffuses. However, in regions of very low-boundary shear stress and turbulence production there may be a net transport radially outward of turbulence generated and transported toward the pipe axis some distance upstream. At larger distances from the wall, in the core of constant turbulence velocities, the longitudinal variations in turbulence intensities produced by variations in turbulence production near the wall are attenuated and are apparently just offset by other effects such as distortion. However, the details of the mechanisms responsible for the constant core are by no means clear. An analysis of the effects of the wall waviness on the turbulence would probably require an extensive numerical treatment of the full turbulence transport equations, along the lines pursued by Harlow & Romero (1969) in their analysis of turbulence distortion in a non-uniform channel. Even then the problem would have to be somewhat simplified. In any case, it appears that rapid distortion theory sheds little light on the turbulence behaviour of wavy-boundary flow.

Boundary drag

It is worthwhile to compare and evaluate the form drag (resulting from the boundary pressure being shifted relative to the boundary wave), shear drag, and head loss over one wavelength for straight and wavy pipes. This comparison is presented in table 2, wherein the various quantities for the wavy pipes were calculated from the experimental data and those for straight pipes were obtained by means of the Kármán–Prandtl friction-factor relation for smooth pipes. The form drag was calculated as the difference between the shear drag obtained from the boundary shear-stress measurements and the pressure-force difference between sections 1 and 9. The comparisons are made for straight pipes with the average and the maximum wavy-pipe diameters. Note that in the case of wavy-

pipe flow the two drag ratios do not sum to the head drop ratio, because the calculation of head loss involves integration of the product of pressure and velocity, both of which are functions of r, over the cross-section. The form drag is seen to be small compared to the shear resistance. It is interesting that in model II the head loss is less than for a straight pipe with the average wavy-pipe diameter. For this long-wave model the diminution in the head loss resulting from the local energy gradient varying approximately as the inverse fifth power of the local diameter (as would be the case if the friction factor were constant along the pipe) more than offsets the increase in energy dissipation engendered by the non-uniformity.

Uniform pipe diameter (ft)	0·446			0·408		
	$(F_f)_w/(F_\tau)_s$	$(F_\tau)_w/(F_\tau)_s$	$(h_f)_w/(h_f)_s$	$(F_f)_w/(F_\tau)_s$	$(F_\tau)_w/(F_\tau)_s$	$(h_f)_w/(h_f)_s$
Model I	0·23	1·41	1·70	0·18	1·09	1·09
Model II	0·20	1·24	1·46	0·16	0·96	0·93

TABLE 2. Comparison of form drag (F_f), shear drag (F_τ), and head drop (h_f) for straight and wavy pipes. The subscripts s and w refer to the straight and wavy pipes, respectively.

5. Analysis

It was observed in section 3 that the radial distribution of longitudinal velocity is well represented by the power law, (1), over some 90 % or more of the radius (see figure 7), but that the reciprocal exponent, n, varies along the pipe (see figure 8). It is possible by means of some simple applications of continuity and energy principles to derive an expression for n, as follows. Assume that at the pipe axis the dissipative stresses are sufficiently small that the total head is constant along the centreline (except, of course, for the gradient due to the energy dissipation of the throughflow); i.e. assume that the boundary waviness does not affect the total head at the centreline. Figure 3 indicates that this is indeed the case. Then it follows that

$$p(x, 0) + \tfrac{1}{2}\rho u_{\max}^2 = C_R, \tag{2}$$

where $p(x, 0)$ is the centreline pressure, ρ is the fluid density, and C_R is a constant for each flow. Integrating (1), weighted by $2\pi r$, from $r = 0$ to $r = r_0(x)$ the resulting expression for the discharge, Q, is

$$Q = 2\pi u_{\max} \int_0^{r_0} r \left(1 - \frac{r}{r_0}\right)^{1/n} dr = 2\pi r_0^2 \frac{n^2}{(n+1)(2n+1)} u_{\max}. \tag{3}$$

Equations (2) and (3) contain three unknowns: n, $u_{\max}$, and $p(x, 0)$. To obtain a third independent relation some results of a potential flow analysis will be utilized.

The velocity potential ϕ describing incompressible potential flow with average velocity U in a circular pipe of average radius R whose longitudinal wall profile is a small-amplitude sinusoid of amplitude a and wave-number k is

$$\phi = \frac{Ua}{I_1(kR)} I_0(kr)\cos(kx), \tag{4}$$

where I is a modified Bessel function of the first kind. The centreline pressure derived from (4) is

$$p(x,0) = C_I - \frac{\rho U^2}{2}\left[1 - 2ka\frac{\sin(kx)}{I_1(kR)}\right], \tag{5}$$

where C_I is an arbitrary constant. It is recognized that the actual flow investigated is far from irrotational, but (5) yields none the less an acceptable approxi-

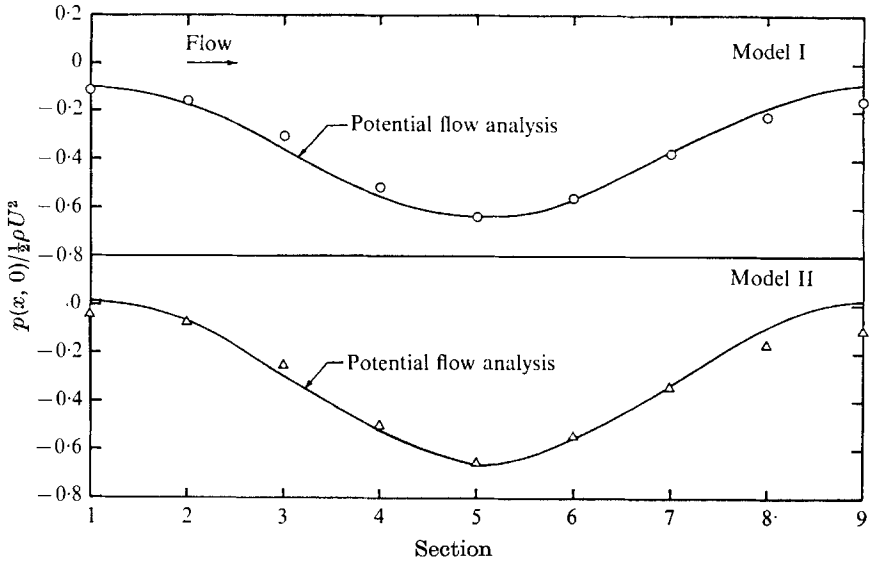

FIGURE 15. Comparison of measured centreline pressures with those computed from potential flow analysis.

mation to the centreline pressure, as is demonstrated in figure 15, which was drawn matching the measured and calculated pressures at section 5 and using the known values of U, a and L. The pressure at other locations in a wavy pipe cannot be predicted from the potential flow model because of the pronounced effect of the velocity profile on the pressure distribution, which was discussed in the preceding section.

Equations (2), (3) and (5) may now be solved for n, with the result

$$\frac{(n+1)(2n+1)}{2n^2} = \frac{r_0^2}{UR^2}\left[C + U^2\left(1 - 2ka\frac{\sin kx}{I_1(kR)}\right)\right]^{\frac{1}{2}}, \tag{6}$$

where $C = 2(C_R - C_I)/\rho$. By substituting the experimentally determined values of n at section 5, the following values of C were determined: model I, $n = 19{\cdot}2$, $C = 0{\cdot}41U^2$; model II, $n = 14{\cdot}2$, $C = 0{\cdot}44U^2$. Using these values of C, the

exponents n were calculated for the other sections, with the results shown in figure 8. The agreement is seen to be as good as could reasonably have been expected in view of the several assumptions utilized. Incidentally, it is interesting to note from (6) that for a flow with $n = 7$ in a uniform pipe ($a = 0$), $C = 0{\cdot}50U^2$. Hence it appears that C decreases with increasing wave steepness.

In the discussion of momentum considerations presented in the preceding section it was noted that the boundary shear stress makes a practically negligible contribution to the momentum balance and plays virtually no role in governing the velocity profiles except, of course, very close to the boundary. The shear stress must, however, still be strongly dependent on the velocity profile, as well as on the boundary divergence and perhaps also on its higher derivatives. It was not found possible in the present study to do better than obtain an empirical expression for the local Darcy–Weisbach friction factor, f, based on the local radius and mean velocity,

$$\left(\frac{f}{8}\right)^{\frac{1}{2}} = \frac{u_\tau}{U_0}, \tag{7}$$

where u_τ and U_0 are the local boundary shear velocity and local mean velocity. The limiting case of this expression for boundary waves of infinite length or zero amplitude is that of a straight pipe. Hence it is in order first to derive an expression between the friction factor, f, and n for steady flow in a straight circular conduit.

Integration of the logarithmic form of the velocity-defect law,

$$\frac{u - u_{\max}}{u_\tau} = \frac{1}{\kappa}\ln\left(1 - \frac{r}{r_0}\right) \tag{8}$$

across the pipe cross-section to obtain a second expression for Q yields

$$Q = 2\pi\int_0^{r_0} r\left[u_{\max} - \frac{u_\tau}{\kappa}\ln\left(1-\frac{r}{r_0}\right)\right]dr = \pi r_0^2\left[u_{\max} - \frac{3}{2}\frac{u_\tau}{\kappa}\right]. \tag{9}$$

Equating (3) and (9) leads to

$$\frac{u_\tau}{\kappa} = U_0(x)\frac{3n+1}{3n^2}, \tag{10}$$

which, after introduction of (7), produces

$$\left(\frac{f}{8}\right)^{\frac{1}{2}} = \kappa\left(\frac{1}{n} + \frac{1}{3n^2}\right). \tag{11}$$

Note that if the second term in parentheses is small compared to the first, (11) reduces to the relation obtained experimentally by Nunner (1956)

$$f^{\frac{1}{2}} = 1/n$$

for $\kappa = 0{\cdot}353$. The empirical expression obtained for the local friction for the case of wavy-pipe flow is

$$f^{\frac{1}{2}} = \frac{1{\cdot}06}{n}\left[1 - 1{\cdot}30\frac{dr_0}{dx}\right]\left[1 \pm 0{\cdot}0103\left|\frac{2\pi}{k}\frac{d^2r_0}{dx^2}\right|^{\frac{1}{2}}\left(\frac{r_0}{\delta_2}\right)^{\frac{3}{2}}\right], \tag{12}$$

where δ_2 is the momentum thickness and is given by

$$\delta_2 = \frac{3r_0 n^2}{2(n+1)(2n+1)(n+2)}$$

for the power-law velocity distribution. The negative and positive signs in (12) correspond to concave and convex boundaries, respectively. The constant 1·06 corresponds for a uniform pipe to $\kappa = 0{\cdot}375$ in (11), the second term of which has been disregarded in its incorporation into (12); note, however, that no assump-

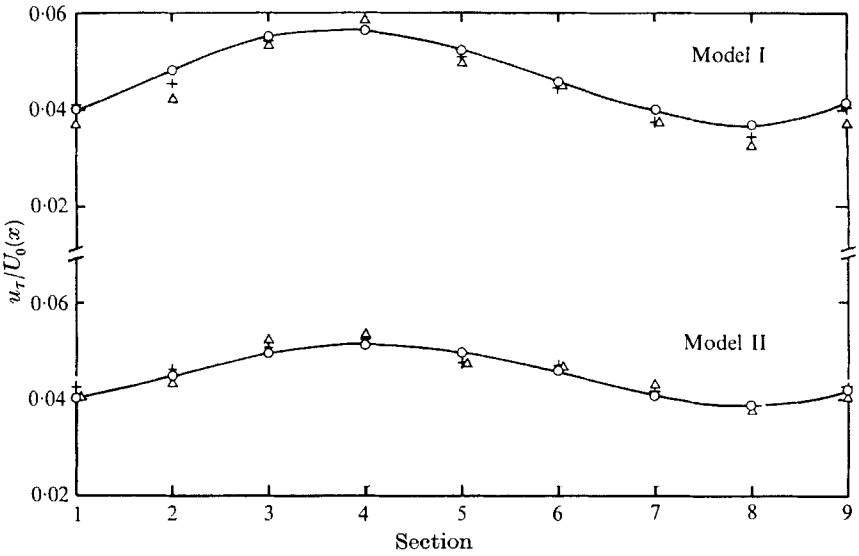

FIGURE 16. Comparison of measured shear velocities and those obtained from (12) and (7) using measured and predicted values of n. ○, from measured shear stress; +, from (12) and (7), measured n; △, from (12) and (7), predicted n.

tion regarding κ for wavy-pipe flows has been included in (12). It is seen that (12) separates the three factors affecting f: the primary flow is reflected in the modified Nunner expression, $1{\cdot}06/n$, to which (12) reduces for $a = 0$; the first term in brackets includes information on the local convergence or divergence of the boundary; and the final term introduces the effect of boundary curvature. Details of the logic used in arriving at (12) are given by Hsu (1968). Figure 16 presents comparisons of values of u_τ/U_0 from the experimental data and those obtained from (12) using both values of n taken from the velocity profiles and computed from (6) using the aforementioned values of C.

In the interest of completing the reporting of results, table 3 summarizes several quantities related to the mean-velocity profiles. The tabulated values of n were obtained from figure 7 and a similar plot for model II. The values of u_τ/U_0 were calculated from the measured boundary shear stress and the mean velocity at each section. Semi-logarithmic plots of the velocity distributions yielded the first set of values of $u_\tau/U_0\kappa$, while the second set was obtained from (10) using the values of n included in table 3; the good agreement between the

two sets of values supports the validity of (10) for the present flow. The values of κ were computed from the reported values of u_τ/U_0 and the values of $u_\tau/U_0\kappa$ obtained from the semi-logarithmic plots of velocity; κ is seen to fluctuate periodically about the uniform-flow value of about 0·40.

Section ...	1	2	3	4	5	6	7	8	9
				Model I					
n	5·3	5·8	8·2	13·9	19·2	13·9	8·2	5·8	5·3
u_τ/U_0	0·040	0·048	0·055	0·056	0·053	0·046	0·040	0·036	0·041
$u_\tau/U_0\kappa$	0·204	0·179	0·122	0·067	0·050	0·067	0·122	0·179	0·204
				(from semi-log plots)					
$u_\tau/U_0\kappa$	0·200	0·182	0·127	0·074	0·053	0·074	0·127	0·182	0·200
				(from (10))					
κ	0·20	0·27	0·45	0·84	1·06	0·69	0·33	0·20	0·20
				Model II					
n	5·7	6·3	8·1	10·9	14·2	10·9	8·1	6·3	5·7
u_τ/U_0	0·040	0·045	0·049	0·051	0·050	0·046	0·041	0·038	0·041
$u_\tau/U_0\kappa$	0·186	0·167	0·126	0·092	0·071	0·092	0·126	0·167	0·186
				(from semi-log plots)					
$u_\tau/U_0\kappa$	0·186	0·167	0·128	0·095	0·072	0·095	0·128	0·167	0·186
				(from (10))					
κ	0·21	0·27	0·39	0·55	0·70	0·50	0·33	0·23	0·22

TABLE 3. Values of $u_\tau/U_0\kappa$ determined from semi-logarithmic plots and computed from (10)

Financial support of this investigation was provided by the Office of Naval Research, Fluid Dynamics Branch, under Contract N00014-68-A-0196-0001. The authors extend grateful acknowledgement to Dr John R. Glover for his considerable assistance in the design and use of the instrumentation.

REFERENCES

BATCHELOR, G. K. & PROUDMAN, I. 1954 The effect of rapid distortion of a fluid in turbulent motion. *Quart. J. Mech. Appl. Math.* **7**, 83–103.

BENJAMIN, T. B. 1959 Shearing flow over a wavy boundary. *J. Fluid Mech.* **6**, 161–205.

BROWN, K. C. & JOUBERT, P. N. 1969 The measurement of skin friction in turbulent boundary layer with adverse pressure gradients. *J. Fluid Mech.* **35**, 737–757.

GLOVER, J. R. 1967 Old gold model, type 4-2H hot-wire anemometer and type 2 mean-product computer. *IIHR Report* 105. Inst of Hydr. Res., The University of Iowa, Iowa City, Iowa.

HARLOW, F. H. & ROMERO, N. C. 1969 Turbulence distortion in a nonuniform tunnel. *Los Alamos Scientific Laboratory Report*, LA-4247.

HSU, S. T. 1968 Turbulent flow in wavy pipes. Ph.D. Thesis, The University of Iowa, Iowa City, Iowa.

IWASA, Y. & KENNEDY, J. F. 1968 Free surface shear flow over a wavy bed. *J. Hydr. Division, ASCE* **94**, HY 2, 431–454.

LARRAS, J. & CLARIA, A. 1960 Wind tunnel research on relative wave and wind action. *L'Houille Blanche*, **6**, 647–677.

LAUFER, J. 1954 The structure of turbulence in fully developed pipe flow. *NACA T.R.* 1174.

MOTZFELD, H. 1937 Die turbulente strömung an welligen wander. *Z. angew. Math. Mech.* **17**, 193–212.

NUNNER, W. 1956 Wärmeübergang und Druckabfall in rauhen Rohren. *VDI-Forschungsheft,* no. 455.

RECHENBERG, I., SCHWEFEL, H. P. & BIENERT, P. 1967 *Messung kleiner Wandschubspannunger bei turbulenten Grenzschichten in Ablösenähe*, Hermann Föttinger Institute für Strömungstenchnik, T.U. Berlin.

RHYMING, I. L. 1963 Non-equilibrium flow inside a wavy cylinder. *J. Fluid. Mech.* **17**, 551–560.

ROBILLARD, L. & KENNEDY, J. F. 1967 Some experimental observations on free surface shear flow over a wavy boundary. *Proc. 12th Congress of IAHR*, Ft. Collins, Colorado.

TAYLOR, G. I. 1935 Turbulence in a contracting stream. *Z. angew. Math. Mech.* **15**, 91–96.

VINCENTI, W. G. 1959 Non-equilibrium flow over a wavy wall. *J. Fluid Mech.* **6**, 481–496.